Research Article Vol. 29, No. 26 / 20 Dec 2021 / Optics Express 43445

Optics EXPRESS

# Multicomponent trace gas detection with hollow-core fiber photothermal interferometry and time-division multiplexing

**FEI LIU,**[1,2] **HAIHONG BAO,**[2,3,5] **HOI LUT HO,**[2,3] **WEI JIN,**[2,3,6] **SHOUFEI GAO,**[4] **AND YINGYING WANG**[4]

[1] *School of Computer and Communication Engineering, University of Science and Technology Beijing, Beijing 100083, China*
[2] *Department of Electrical Engineering and Photonics Research Institute, The Hong Kong Polytechnic University, Hong Kong 518060, China*
[3] *Photonics Research Center, The Hong Kong Polytechnic University Shenzhen Research Institute, Shenzhen 518057, China*
[4] *Institute of Photonics Technology, Jinan University, Guangzhou 510632, China*
[5] *haihong.bao@polyu.edu.hk*
[6] *eewjin@polyu.edu.hk*

**Abstract:** We report a multicomponent photothermal gas sensor with a conjoined-tube hollow-core optical fiber gas cell. With a common Fabry-Perot probe interferometer and a common gas cell, simultaneous detection of methane, acetylene and ammonia can be achieved by time-division multiplexing. Experiments with a 15-cm-long hollow-core fiber demonstrated noise-equivalent concentration of 24.2 parts-per-billion (ppb) for methane, 11.6 ppb for acetylene, and 46.1 ppb for ammonia. The dynamic range is measured to be around 5 orders of magnitude. The crosstalk issue is addressed by spectrum fitting. Assisted with an air pump and a compact gas chamber, the response time of less than 10 s is achieved.

## 1. Introduction

Trace gas detection is of importance in various fields including atmospheric chemistry [1,2], energy industry [3,4], and medical research [5,6]. These applications often require the detection of multiple gas species down to parts-per-billion (ppb) level or lower. Among the various gas detection technologies, laser absorption spectroscopy offers unique advantages in specificity by utilizing the "finger-print" absorption features of gas molecules [7]. Recently optical fiber spectroscopic gas sensors with hollow-core fibers (HCFs) as sensing elements (gas cells) have been developed, demonstrating the merits of simple optical construction and remote detection capability [8].

Photothermal interferometry (PTI), a derivative of laser absorption spectroscopy, is a highly sensitive technique for trace gas detection. A modulated pump beam with wavelength tuned to a molecular absorption line heats up the gas medium and modulates its local refractive index (RI) distribution. This modulates the phase of a probe beam propagating in the medium, which is detected by optical interferometry [9]. The advantage of the pump-probe approach is that the probe wavelength can be selected to be in the near-infrared (NIR) telecom band where mature and cost-effective fiber-optic components are available, enabling sophisticated interferometric circuits to achieve high sensitivity with compact size.

With HCF gas cells and optimized phase detection schemes, the noise-equivalent concentration (NEC) of PTI systems has reached the level of ppb and sub-ppb [10,11] for a variety of gas species, including methane [12,13], ethane [14], acetylene [15,16], carbon monoxide [17], etc. However, these reported systems are for the detection of a single gas component. In this paper,

#446478 https://doi.org/10.1364/OE.446478
Journal © 2021 Received 21 Oct 2021; revised 25 Nov 2021; accepted 29 Nov 2021; published 13 Dec 2021

we report an optical fiber PTI system capable of detecting multiple gases simultaneously. The system uses a single HCF gas cell, a common probe interferometer for phase detection, and time-division multiplexing of different pump laser sources to recover concentrations of different gas components. As an example, we experimentally demonstrate simultaneous detection of three gases, i.e., methane ($CH_4$), acetylene ($C_2H_2$) and ammonia ($NH_3$), down to the level of ppb.

## 2. Principle and experimental setup

Figure 1 shows the configuration of the PTI system. The gas cell is made of a 15-cm-long hollow-core conjoined-tube fiber (CTF) with its cross-sectional image and spectral transmission shown in Fig. 2(a). The CTF has a low-loss (<17 dB/km) transmission window from 1300 nm to 1700nm [18], covering the probe wavelength (~1550 nm) as well as the pump wavelengths (~1531 nm and ~1651 nm) used in our experiments. Other types of hollow core fibers may also be used, as long as they support low loss transmission of the pump and probe at the same time. The CTF is mechanically spliced to lead in/out single mode fiber (SMF) pigtails using ceramic ferrules and sleeves. With help of optical microscope, an air gap of ~1 µm between CTF and SMF is formed for gas filling. The CTF gas cell is housed within a gas chamber, which is sealed up with UV glue. Gas inlet and outlet are equipped on the gas chamber and the outlet is connected to an air pump to speed up gas filling during experiment.

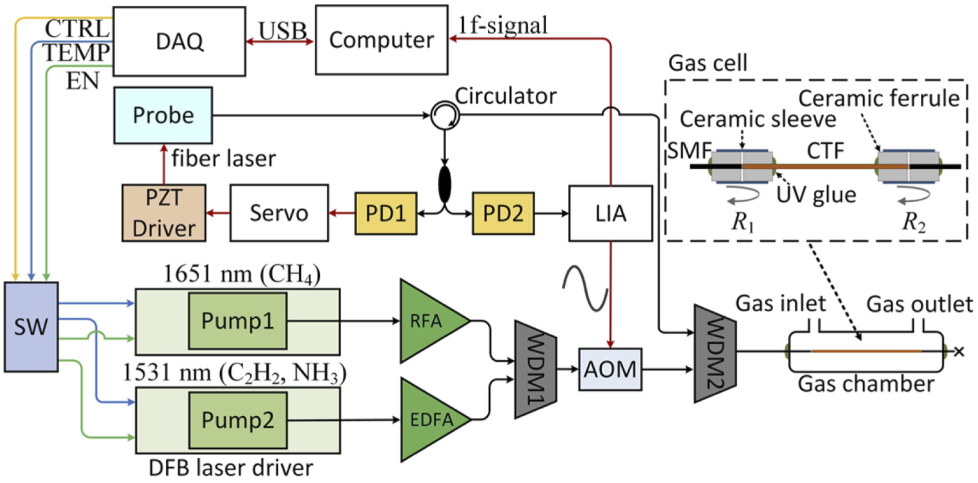

**Fig. 1.** Schematic of the multicomponent trace gas sensor system. SW, switch; RFA, Raman fiber amplifier; EDFA, Erbium-doped fiber amplifier; AOM, acousto-optic modulator; WDM1 and WDM2, wavelength-division multiplexers; PD1 and PD2, photodetectors; LIA, lock-in amplifier; DAQ, data acquisition card; PZT, piezoelectric transducer.

The natural reflections ($R_1 \approx R_2 \approx 4\%$) at the SMF/CTF joints form a low-finesse Fabry-Perot interferometer (FPI), and the reflected probe light intensity from the FPI can be written as

$$I = I_0[1 + v\cos(\varphi(t) + \varphi_0)], \tag{1}$$

where $I_0$ is the incident probe light intensity, $v$ is the fringe visibility which is determined by the reflectance at the joints and the loss of the CTF. $\varphi_0$ is a DC phase bias that determines the operating point, at which the small photothermal phase modulation $\varphi(t)$ due to gas absorption is converted to intensity modulation at the FPI output.

By detecting the DC component using PD1 and feeding it to servo control the wavelength of the probe fiber laser via a PZT driver, the FPI can be stabilized at quadrature (i.e. $\varphi_0 = \pi/2$). Then

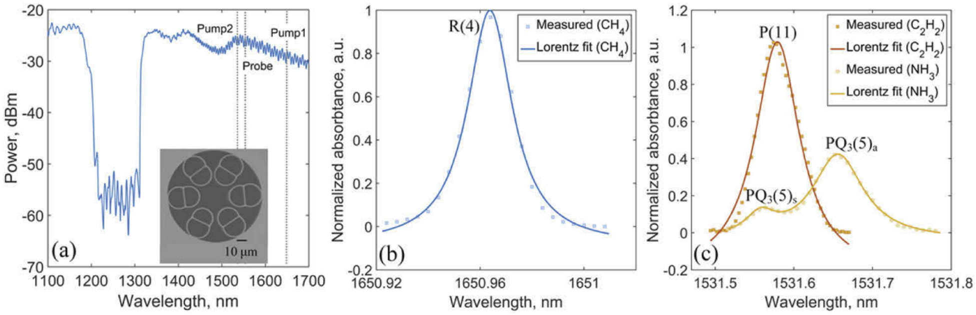

**Fig. 2.** (a) The cross-section image and spectral transmission of the 15-cm-long CTF. (b) Measured and Lorentzian fitting absorption spectrum around 1650.96 nm for $CH_4$ detection. (c) Measured and Lorentzian fitting absorption spectrum from 1531.5 nm to 1531.8 nm for $C_2H_2$ and $NH_3$ detection.

the AC component of the reflected probe light intensity ($\Delta I(t)$) is linearly proportional to the photothermal phase modulation $\Delta\varphi(t)$

$$\Delta I(t) \approx I_0 \nu \Delta\varphi(t), \tag{2}$$

where we have assume that $\Delta\varphi(\mathrm{t}) <<1$, which can be expressed as [10]

$$\Delta\varphi(t) = k\alpha(\lambda_{pump})CLP_{pump}, \tag{3}$$

where $C$ is the gas concentration, $L$ the length of the CTF, $P_{pump}$ the pump power in the CTF and $\alpha(\lambda_{pump})$ the gas absorption coefficient. The photothermal phase modulation is linearly proportional to the gas concentration, which can be recovered by demodulating PD2 output with a lock-in amplifier (LIA).

The absorption lines used in our experiment are the R(4) line of $CH_4$ at 1650.96 nm, the P(11) line of $C_2H_2$ at 1531.58 nm, and the $PQ_3(5)_a$ line of $NH_3$ around 1531.65 nm [19]. The measured spectrum around the absorption lines of the three gas species are shown in Figs. 2(b) and 2(c). The measured data were obtained using fiber-coupled reference cells of $CH_4$, $C_2H_2$ and $NH_3$ (Wavelength references Inc.) and have been normalized. Figures 2(b) and 2(c) also show the Lorentzian fitting curves of the measured data, in good agreement with the center wavelength determined using the HITRAN database. The experiments are conducted at atmospheric pressure and hence collision broadening is dominant [20], which results a Lorentzian absorption lineshape [21]. Note that the spectrum of $NH_3$ has two peaks with the left peak (the P(11) line of $C_2H_2$ at 1531.58 nm, and the $PQ_3(5)_s$) overlapping with that of $C_2H_2$ (Fig. 2(c)), leading to crosstalk, which will be addressed in a later section. A distributed feedback (DFB) laser, i.e., Pump1, is used to detect $CH_4$. As the selected absorption lines of $C_2H_2$ and $NH_3$ are very close (within 0.2 nm) to each other, these two gases are detected using the same DFB laser, i.e., Pump2. The power levels of Pump1 and Pump2 are boosted to ~300 mW by a Raman fiber amplifier (RFA, custom made by Amonics Ltd. [12]) and an Erbium-doped fiber amplifier (EDFA, AEDFA-BO-23, Amonics Ltd.), respectively. The amplified pump beams are firstly combined by a wavelength-division multiplexer (WDM1) and then sinusoidally modulated in intensity by an acousto-optic modulator (AOM). The modulated pump beams are combined with a 1550 nm probe beam by WDM2 and guided into the CTF gas cell. Compared with wavelength modulation by injection current [14], the external acousto-optic modulation generates a simple 1f photothermal signal that follows the same Lorentzian function of the absorption line. This benefits the curve fitting in determining the concentrations of two gases with overlapping absorption lines, as will be discussed in the later section. The probe is from a fiber laser (CoSF-D-EY-M, Connect Laser Technology Co., Ltd.)

with linewidth of <10 kHz and equipped with a piezoelectric stretcher for wavelength tuning. The reflected probe beam from the gas cell is guided back through the same port of WDM2 and used for FPI stabilization and detection of the photothermal phase modulation via a lock-in amplifier (LIA).

Simultaneous detection of multiple gas species is implemented via an electrical switch (SW, COMS analog multiplexer, XD4053). It guides the enable signal ("EN") as well as the temperature tuning signal ("TEMP") to one of the pump laser drivers according to the digital control signal ("CTRL"). When "CTRL" is 0 (or 1), the input signal ("TEMP" and "EN") is switched to pump driver 1 (or pump driver 2). The pump emission is enabled when "EN" is at a high voltage and disabled when "EN" is at a low voltage. "TEMP" is set as sawtooth waveform that tunes the working temperature of the pump laser. All the signals of "EN", "TEMP" and "CTRL" are generated by a computer via the data acquisition card (DAQ).

## 3. Experiment results and discussion

Gas detection experiments were conducted by filling different concentrations of target gases (balanced with $N_2$) into the gas chamber through flowmeters. The modulation frequency applied on the AOM is 26 kHz. Figure 3(a) plots "CTRL", "TEMP" waveforms and the R-values of first harmonic (1f) of the LIA output when the gas chamber was filled with 1000 part-per-million (ppm) $CH_4$, $C_2H_2$ and $NH_3$, respectively, under lab environment. The LIA time constant is 1 s with filter slope of 24 dB/Oct. To achieve time-division multiplexing, "CTRL" was set at 0 for $CH_4$ detection and 1 for $C_2H_2$ and $NH_3$ detection as shown in the up panel of Fig. 3(a). The peak amplitude of temperature tuning signal ("TEMP") is 4.5 V with a scanning period of 100 s, as shown in the middle panel of Fig. 3(a). This enables the tuning of pump wavelengths across the selected gas absorption lines. The R-values of the 1f-LIA output for the three different gases are plotted in the bottom panel of Fig. 3(a). It can be seen that the 1f-LIA output of $CH_4$ and $C_2H_2$ demonstrate Lorentz profile, while that for $NH_3$ shows a superposition of two Lorentz profiles. The peak value of the 1f-LIA output in a scanning period is read out as the 1f signal amplitude.

The noise levels were evaluated fixing the pump wavelengths respectively at the corresponding absorption line centers and with the gas chamber filled with pure $N_2$. The two-minute-long noise records for the three gases are shown in Fig. 3(b). We use standard deviation (std.) to characterize the noise level. The signal amplitudes of LIA output, std. of noise, NEC and noise equivalent absorption (NEA) for signal-to-noise ratio of unity are summarized in Tab. 1. The results show that this system achieves NECs of 24.2 ppb, 11.6 ppb and 46.1 ppb for $CH_4$, $C_2H_2$ and $NH_3$ respectively. The NEA for the three gases are, respectively, $7.43\times10^{-9}$ cm$^{-1}$, $1.35\times10^{-8}$ cm$^{-1}$ and $9.87\times10^{-9}$ cm$^{-1}$. The high performance is attributed to the ultra-sensitive all-fiber PTI and the strong light-gas interaction in the hollow core fiber. Figure 3(c) depicts the Allan deviation plot using the noise data over 4 hours for $CH_4$ detection. The optimal average time is ~450 s with a std. of 0.086 µV (mean value for integration time from 400 s to 600 s, as shown in Fig. 3(c)), corresponding to a NEC of ~3.7 ppb. Similarly, the Allan deviation analyses for $C_2H_2$ and $NH_3$ indicate that the best achievable NECs are 2.0 ppb for $C_2H_2$ and 7.0 ppb for $NH_3$. These results are comparable to that single component gas sensors [16].

**Table 1. The signal amplitude, std. of noise, NEC and NEA for the three gases under test. The concentrations of the gas samples are 1000 ppm.**

| gas | signal amplitude, mV | std. of noise[a], µV | NEC, ppb | NEA, cm$^{-1}$ |
|---|---|---|---|---|
| $CH_4$ | 23.6 | 0.57 | 24.2 | $7.43\times10^{-9}$ |
| $C_2H_2$ | 57.8 | 0.67 | 11.6 | $1.35\times10^{-8}$ |
| $NH_3$ | 21.7 | 1.10 | 46.1 | $9.87\times10^{-9}$ |

[a] The noise were measured with the gas cell filled with pure $N_2$.

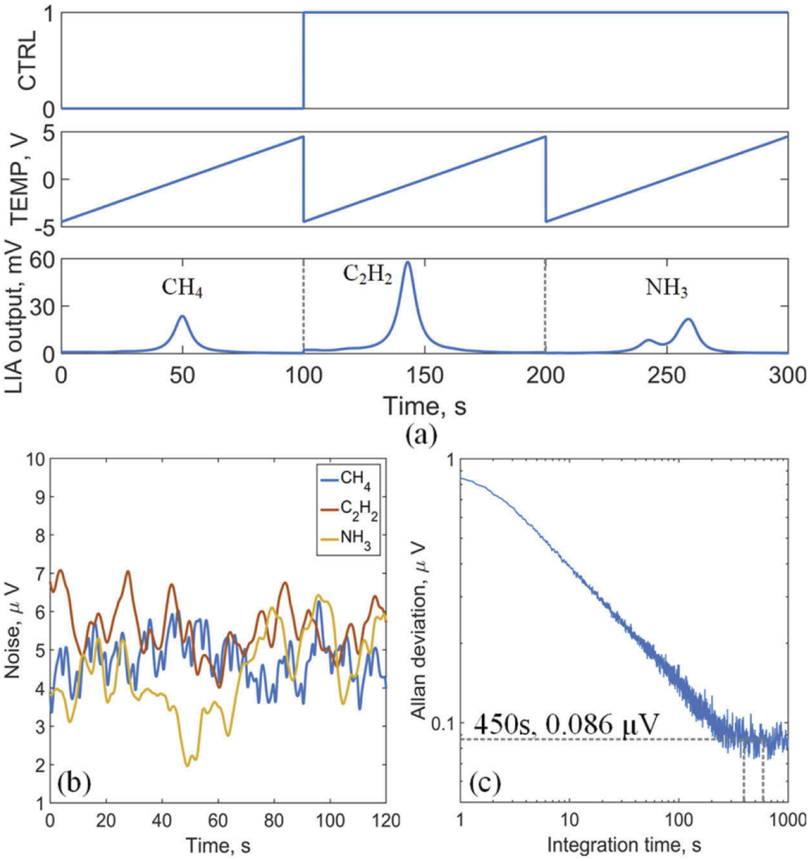

**Fig. 3.** (a) The "CTRL" value (up panel), "TEMP" signal (middle panel) and R-value of the 1f signal (bottom panel) for 1000 ppm of $CH_4$, $C_2H_2$ and $NH_3$ balanced in $N_2$; (b) Noise waveforms when the gas chamber is filled with pure $N_2$ and the pump wavelength is fixed at the absorption line center; (c) Allan deviation of the baseline noise over 4 hours for $CH_4$ detection.

The values of LIA output at different gas concentrations are plotted, in Fig. 4(a), as circles, squares and diamonds for the three different gases. The inset figure demonstrates the results within the concentration from 0 to 20 ppm in a log scale. The lines are the linear fitting results. The measured data of all the gases present good linearity with the R-square value of 0.9997 for $CH_4$, 0.9998 for $C_2H_2$ and 0.9995 for $NH_3$ respectively. The dots at bottom left indicate the derived NEC values from the std. of noise levels. It is hard to prepare gas samples with such a low concentration using the flowmeters in our lab and hence we plot the fitting results using the dashed lines. Figure 4(b) plots the actual 1f signals of $CH_4$ samples with concentrations of 1 ppm, 100 ppm and 10 000 ppm. It can be seen that the peak value of the 1f signal increases linearly with concentration. When the gas concentration is low, e.g. 1 ppm, the influence of noise is more obvious than the cases with higher concentrations.

From the data in Fig. 4(a), the dynamic ranges, which is defined as $20\log_{10}(C_{\max}/\mathrm{NEC})$ ($C_{\max}$ is the maximum gas concentration used in experiment), are 112 dB, 99 dB and 86 dB for $CH_4$, $C_2H_2$ and $NH_3$. These values demonstrate that the dynamic ranges for the detection of the three gases are about 5 orders of magnitude. The smaller range for $NH_3$ detection is due to the relatively larger values of the NEC, caused by the weaker absorption coefficient of the selected line. Actually, the maximum gas concentrations we tested are limited by the available

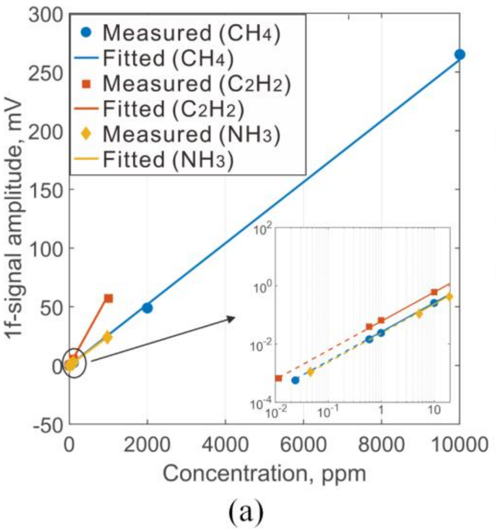

**Fig. 4.** (a) The values of 1f signals as function of gas concentrations; (b) The measured 1f signals of $CH_4$ samples with concentrations of 1 ppm, 100 ppm and 10 000 ppm.

high-concentration gas samples in our lab, instead of the capability of the PTI system, meaning that the authentic dynamic range is larger than that presented above.

The selection of the absorption lines for $C_2H_2$ and $NH_3$ detection means cross sensitivity is inevitable and needs to be dealt with. Here, the spectrum fitting method is adopted to determine the concentrations of these two gases. Firstly, the 1f photothermal spectrums of calibrated 1000 ppm $C_2H_2$ in $N_2$ and 1000 ppm $NH_3$ in $N_2$ were obtained experimentally. These spectrums are normalized by gas concentrations and fitted to a Lorentzian function and a superposition of two Lorentzian functions, respectively. The fitted functions are denoted as $f_1(t)$ and $f_2(t)$, representing the line shapes of $C_2H_2$ and $NH_3$, respectively, as shown in Fig. 5(a).

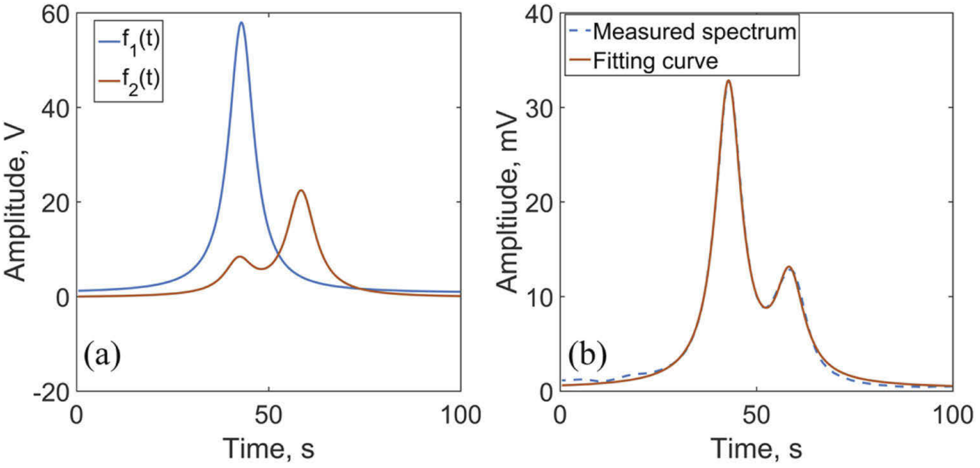

**Fig. 5.** (a)The fitting line shapes of the photothermal spectrums of $C_2H_2$ ($f_1(t)$, blue curve) and $NH_3$ ($f_2(t)$, red curve). (b) The measured (dashed blue curve) and fitting spectrum (solid red curve) of the gas mixture with 500 ppm $C_2H_2$ and 500 ppm $NH_3$.

For a mixed sample of $C_2H_2$ and $NH_3$, the measured photothermal spectrum is denoted as $f(t)$. A set of coefficients ($C_1$ and $C_2$) may be found by minimizing the expression

$$\varepsilon = \int_{t=0}^{T} [f(t) - (C_1 f_1(t) + C_2 f_2(t))]^2 dt, \tag{4}$$

where $T$ is the scanning period and is 100 s in the experiment. Then, the concentrations of $C_2H_2$ and $NH_3$ are respectively $C_1$ and $C_2$. Figure 5(b) shows the experiment results when a gas mixture of 500 ppm $C_2H_2$ and 500 ppm $NH_3$ in $N_2$ is in the gas cell. The dashed blue curve is the measured spectrum whereas the solid red curve is the fitted curve. The fitting spectrum agrees well with measured spectrum, indicating that this method addresses the crosstalk problem well. The solved concentration are $C_1$=496 ppm ($C_2H_2$) and $C_2$=492 ppm ($NH_3$) respectively. Note that if the crosstalk were not taken into consideration, the concentration values obtained by direct peak measurement are 556 ppm for $C_2H_2$ and 830 ppm for $NH_3$. These large deviations are unacceptable for applications that require ultrasensitive trace gas detection, e.g. atmospheric and planetary monitoring [22] and breath diagnostics [23]. Fortunately the spectrum fitting method improves the accuracy of the concentration measurement significantly. Thus, we can see that, beside the capability of detecting multiple components in a gas mixture with one compact gas cell, the system also demonstrates the ability to reduce the crosstalk when two gases having overlapped absorption lines, which is important for practical applications.

When the wavelength of the pump lasers are fixed at the absorption line by setting the “TEMP” signal at a specific DC value, the sensor can record the dynamic process of the 1f signal amplitude variation. The settings of LIA are the same, i.e. the time constant is 1 s and the filter slope is 24 dB/Oct. Figure 6 shows the recorded 1f signal amplitude during a filling-in and pumping-out process using 100 ppm $CH_4$. The gas sample was filled into the pre-vacuum gas chamber at 5 s and it took about 6.4 s from 10% to 90% of the maximum value. The amplitude was kept at ~2.5 mV for 10 s, then the air pump was switched on. The amplitude began to fall down with a falling time of 6.7 s (90% to 10%). Assisted by the air pump and the compact gas chamber (the volume is only ~86.4 mL), the dynamic response is much faster than the previous work whose rising time is ~300 s [14].

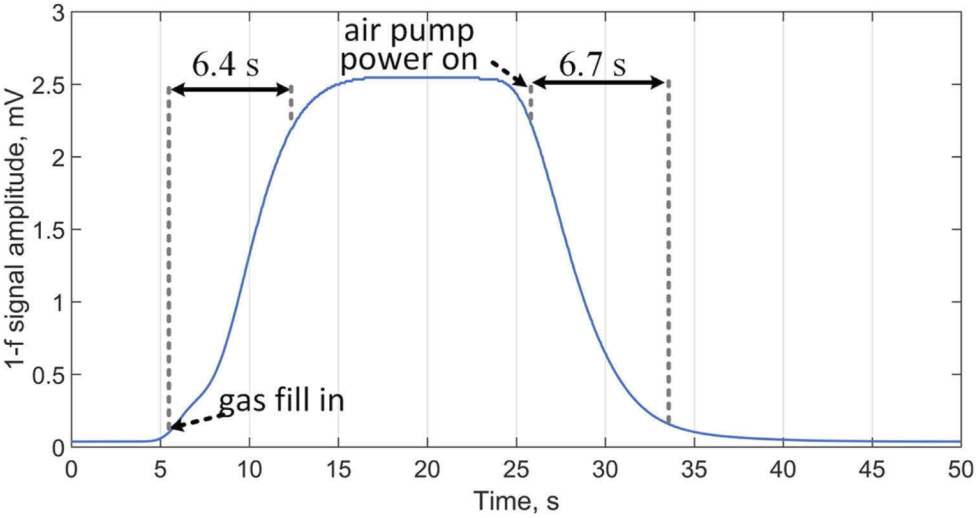

**Fig. 6.** The recorded 1f signal amplitude variation during the filling-in and pumping-out process using 100 ppm $CH_4$.

## 4. Conclusion

We have demonstrated a time-division multiplexed multicomponent trace gas sensor system. The system uses multiple pump laser sources for the detection of different gases but shares a common CTF gas cell and probe interferometric detection circuitry, reducing the overall cost of the system. The system achieved NEC of 24.2 ppb, 11.6 ppb and 46.1 ppb for $CH_4$, $C_2H_2$ and $NH_3$, respectively. The dynamic range is about 5 orders of magnitude for all of the three types of gases and has rooms for further improvement. The crosstalk in $C_2H_2$ and $NH_3$ detection, due to overlapping of the selected absorption lines, is addressed by the method of spectrum fitting. The response time is reduced to less than 10 s with an auxiliary air pump. This all-fiber system has the advantages of high sensitivity, large dynamic range, rapid response, and cost-effectiveness, accelerating the field application of PTI-based gas sensors.

**Funding.** Local Innovative and Research Teams Project of Guangdong Pear River Talents Program (2019BT02X105); Hong Kong SAR Government GRF Grant (PolyU 152206/17E); National Natural Science Foundation of China (61827820, 61905004); Hong Kong Polytechnic University (W151, YW4C).

**Disclosures.** The authors declare no conflicts of interest.

**Data availability.** Data is available from the authors upon reasonable request.

### References

1. Y. Xiao, J. A. Logan, D. J. Jacob, R. C. Hudman, R. Yantosca, and D. R. Blake, "Global budget of ethane and regional constraints on U.S. sources," J. Geophys. Res. **113**(D21), D21306 (2008).
2. I. J. Simpson, F. S. Rowland, S. Meinardi, and D. R. Blake, "Influence of biomass burning during recent fluctuations in the slow growth of global tropospheric methane," Geophys. Res. Lett. **33**(22), L22808 (2006).
3. M. B. Frish and D. M. Sonnenfroh, "Trace Gas Analyzers Based on Tunable Diode Laser Absorption Spectroscopy (TDLAS) for Energy Production, Transmission, and Storage," *Optics and Photonics for Advanced Energy Technology*. Optical Society of America, 2009: ThB3.
4. B. Hirst, G. Gibson, S. Gillespie, I. Archibald, O. Podlaha, K. D. Skeldon, J. Courtial, S. Monk, and M. Padgett, "Oil and gas prospecting by ultra-sensitive optical gas detection with inverse gas dispersion modelling," Geophys. Res. Lett. **31**(12), L12115 (2004).
5. C. B. de Lacy, M. Ledochowski, and N. M. Ratcliffe, "The importance of methane breath testing: a review," J. Breath Res. **7**(2), 024001 (2013).
6. P. Paredi, S. A. Kharitonov, and P. J. Barnes, "Elevation of exhaled ethane concentration in asthma," Am. J. Respir. Crit. Care Med. **162**(4), 1450–1454 (2000).
7. J. Hodgkinson and R. P. Tatam, "Optical gas sensing- a review," Meas. Sci. Technol. **24**(1), 012004 (2013).
8. W. Jin, H. L. Ho, Y. C. Cao, J. Ju, and L. F. Qi, "Gas detection with micro- and nano-engineered optical fibers," Opt. Fiber Technol. **19**(6), 741–759 (2013).
9. S. E. Bialkowski, *Photothermal Spectroscopy Methods for Chemical Analysis* (John Wiley & Sons, 1996), vol. 177.
10. W. Jin, Y. Cao, F. Yang, and H. L. Ho, "Ultra-sensitive all-fibre photothermal spectroscopy with large dynamic range," Nat. Commun. **6**(1), 6767 (2015).
11. P. Zhao, Y. Zhao, H. Bao, H. L. Ho, W. Jin, S. Fan, S. Gao, Y. Wang, and P. Wang, "Mode-phase-difference photothermal spectroscopy for gas detection with an anti-resonant hollow-core optical fiber," Nat. Commun. **11**(1), 1–8 (2020).
12. P. Zhao, H. L. Ho, W. Jin, S. Fan, S. Gao, and Y. Wang, "Hollow-core fiber photothermal methane sensor with temperature compensation," Opt. Lett. **46**(11), 2762–2765 (2021).
13. G. Gomolka, M. Krajewska, A. M. Khegai, S. V. Alyshev, A. S. Lobanov, S. V. Firstov, D. Pysz, G. Stepniewski, R. Buczynski, M. Klimczak, and M. Nikodem, "Heterodyne photothermal spectroscopy of methane near 1651 nm inside hollow-core fiber using a bismuth-doped fiber amplifier," Appl. Opt. **60**(15), C84–C91 (2021).
14. F. Chen, S. Jiang, W. Jin, H. Bao, H. L. Ho, C. Wang, and S. Gao, "Ethane detection with mid-infrared hollow-core fiber photothermal spectroscopy," Opt. Express **28**(25), 38115–38126 (2020).
15. Y. Lin, F. Liu, X. He, W. Jin, M. Zhang, F. Yang, H. L. Ho, Y. Tan, and L. Gu, "Distributed gas sensing with optical fibre photothermal interferometry," Opt. Express **25**(25), 31568–31585 (2017).
16. H. Bao, Y. Hong, W. Jin, H. L. Ho, C. Wang, S. Gao, Y. Wang, and P. Wang, "Modeling and performance evaluation of in-line Fabry-Perot photothermal gas sensors with hollow-core optical fibers," Opt. Express **28**(4), 5423–5435 (2020).
17. C. Yao, Q. Wang, Y. Lin, W. Jin, L. Xiao, S. Gao, Y. Wang, P. Wang, and W. Ren, "Photothermal CO detection in a hollow-core negative curvature fiber," Opt. Lett. **44**(16), 4048–4051 (2019).
18. S. Gao, Y. Wang, W. Ding, D. Jiang, S. Gu, X. Zhang, and P. Wang, "Hollow-core conjoined-tube negative-curvature fibre with ultralow loss," Nat. Commun. **9**(1), 1–6 (2018).

19. L. Lundsbergnielsen, F. Hegelund, and F. M. Nicolaisen, “Analysis of the high-resolution spectrum of ammonia ($^{14}NH_3$) in the near-infrared region, 6400-6900 $cm^{-1}$,” J. Mol. Spectrosc. **162**(1), 230–245 (1993).
20. Y. Lin, “Photothermal gas spectroscopy with hollow-core photonic bandgap fibre: from fundamental mechanism to distributed sensing application,” Ph.D. thesis (Department of Electrical Engineering, The Hong Kong Polytechnic University, 2018), pp. 30.
21. T. Svensson and Z. Shen, “Laser spectroscopy of gas confined in nanoporous materials,” Appl. Phys. Lett. **96**(2), 021107 (2010).
22. P. Laj, J. Klausen, M. Bilde, C. Plaß-Duelmer, G. Pappalardo, C. Clerbaux, U. Baltensperger, J. Hjorth, D. Simpson, S. Reimann, P. F. Coheur, A. Richter, M. De Mazière, Y. Rudich, G. McFiggans, K. Torseth, A. Wiedensohler, S. Morin, M. Schulz, J. D. Allan, J. L. Attié, I. Barnes, W. Birmili, J. P. Cammas, J. Dommen, H. P. Dorn, D. Fowler, S. Fuzzi, M. Glasius, C. Granier, M. Hermann, I. S. A. Isaksen, S. Kinne, I. Koren, F. Madonna, M. Maione, A. Massling, O. Moehler, L. Mona, P. S. Monks, D. Müller, T. Müller, J. Orphal, V. H. Peuch, F. Stratmann, D. Tanré, G. Tyndall, A. Abo Riziq, M. Van Roozendael, P. Villani, B. Wehner, H. Wex, and A. A. Zardini, “Measuring atmospheric composition change,” Atmos. Environ. **43**(33), 5351–5414 (2009).
23. D. Smith and P. Španěl, “The challenge of breath analysis for clinical diagnosis and therapeutic monitoring,” Analyst **132**(5), 390–396 (2007).